Two-color electromagnetically induced transparency via modulated coupling between a mechanical resonator and a qubit

Xin Wang,[1,2] Adam Miranowicz,[2,3] Hong-Rong Li,[1] Fu-Li Li,[1] and Franco Nori[2,4]

[1]*Institute of Quantum Optics and Quantum Information, School of Science, Xi'an Jiaotong University, Xi'an 710049, China*
[2]*Theoretical Quantum Physics Laboratory, RIKEN Cluster for Pioneering Research, Wako-shi, Saitama 351-0198, Japan*
[3]*Faculty of Physics, Adam Mickiewicz University, 61-614 Poznań, Poland*
[4]*Physics Department, The University of Michigan, Ann Arbor, Michigan 48109-1040, USA*

We discuss level splitting and sideband transitions induced by a modulated coupling between a superconducting quantum circuit and a nanomechanical resonator. First, we show how to achieve an unconventional time-dependent longitudinal coupling between a flux (transmon) qubit and the resonator. Considering a sinusoidal modulation of the coupling strength, we find that a first-order sideband transition can be split into two. Moreover, under the driving of a red-detuned field, we discuss the optical response of the qubit for a resonant probe field. We show that level splitting induced by modulating this longitudinal coupling can enable two-color electromagnetically induced transparency (EIT), in addition to single-color EIT. In contrast to standard predictions of two-color EIT in atomic systems, we apply here only a single drive (control) field. The monochromatic modulation of the coupling strength is equivalent to employing two eigenfrequency-tunable mechanical resonators. Both drive-probe detuning for single-color EIT and the distance between transparent windows for two-color EIT can be adjusted by tuning the modulation frequency of the coupling.

I. INTRODUCTION

Superconducting quantum circuits (SQCs) [1–8] are ideal artificial platforms for studying microwave photonics [9] even in the ultrastrong light-matter coupling regime [10]. Many quantum-optical effects, such as quantum Rabi oscillations [11,12], electromagnetically induced transparency (EIT) [13–18], Autler-Townes splitting [19–22], and photon blockade [23,24], have been successfully demonstrated with SQCs.

In contrast to natural atoms and optical cavities, the basic elements (i.e., multilevel superconducting systems and resonators) in SQCs can freely be designed and controlled for various purposes in microwave photonics [9] and quantum-information technologies [25].

Most commonly, the coupling between a superconducting qubit and a single-mode microwave resonator field is transverse [9,26], where the dipole moment of the qubit interacts with the electric (or magnetic) field of the resonator mode, and therefore being an exact analog of the standard quantum Rabi model in cavity quantum electrodynamics (QED) experiments [27]. The quantum dynamics of such systems has been extensively studied for decades due to its potential applications in, e.g., quantum information processing and quantum optics [28–32].

In recent years, some theoretical and experimental research studies have been devoted to SQCs with another type of interaction form, i.e., the so-called *longitudinal* coupling [33–37]. In a circuit-QED system with *longitudinal* interaction, the qubit-transition frequency is modulated by a quantized field, and the Pauli σ_z qubit operator couples with a quadrature field operator [37]. Compared with the transverse coupling [38], the longitudinal coupling has its inherent advantages since the interaction term commutes with the qubit operator σ_z. For

example, there is no Purcell decay and residual interactions between a qubit and its resonator. By using SQCs with longitudinal coupling, one can realize various quantum-control tasks, such as error-correction codes [39,40] or multiexcitation generation [12,40–42] among many other applications [9].

Recently, several studies have been focused on systems with parametrically modulated *longitudinal* coupling, where the interaction strength was rather not constant but modulated in time at certain frequencies. This modulated interaction can be viewed as a qubit-state-dependent drive on a resonator. If the modulation rate is equal to the resonator frequency, qubit states can be read out rapidly via quantum nondemolition (QND) measurements [43]. Moreover, it is possible to obtain a high-fidelity controlled-phase gate, if modulating the longitudinal coupling between two remote qubits and a common resonator [44]. All these studies indicate that the *modulated longitudinal* coupling has its own advantages over the transverse and *constant* longitudinal interactions, and provides another way to achieve better quantum control and engineering. However, as discussed in Refs. [43,45,46], it is not easy to obtain such modulated couplings in either natural or artificial systems.

In this paper, we describe possible sideband transitions and the optical response in a system with a parametrically modulated longitudinal coupling which, to our knowledge, has not been discussed in previous studies. We start our discussions by proposing two possible circuit layouts, where superconducting qubits are longitudinally coupled to nanomechanical resonators (NAMRs) via an external flux [47]. The coupling can be conveniently modulated in time by changing external magnetic fields. Considering a transverse driving field of a qubit, we find that a sideband transition can be split into several asymmetric parts if the modulation is sinusoidal.

Assuming that a resonant probe field is also applied to a qubit, we demonstrate that both single- and two-color (bichromatic) EIT [48–50] can be observed. For single-color EIT, parametric modulation is equal to a flexible NAMR with a tunable eigenfrequency and, therefore, the drive-probe detuning of the EIT dip can be conveniently tuned. For two-color EIT, two transparent windows result from the parametric modulation of the longitudinal coupling, and the distance between two transparent windows can be adjusted by changing the modulation frequency, rather than sweeping two control frequencies in a conventional bichromatic EIT system [50–52].

There are various potential applications of EIT based on circuit-QED systems, such as optical switching [9,53,54], controlling slow light for information storage, demonstrating single-photon router devices [55,56], and controlling photon transmission through a circuit-QED system [57,58]. Two-color EIT can be employed for entangling photons via cross-phase modulation and slowing photons at different frequencies [51,59,60]. Our results can be helpful to study the dynamics for systems with time-dependent longitudinal coupling, and applications based on EIT in microwave photonics [9].

The outline of the paper is as follows. In Sec. II, we describe a possible approach to mediate a flux (transmon) qubit with a NAMR via a modulated longitudinal coupling. In Sec. III, we derive an analytical Hamiltonian describing sideband-transition splitting. In Sec. IV, we discuss single- and two-color EIT, and show how to tune these two effects by changing drive-field parameters. Our final discussions and conclusions are presented in Sec. V.

II. MODEL

A possible circuit-QED implementation of the time-dependent longitudinal interaction has been discussed in Ref. [43]. Specifically, a transmon qubit was assumed to interact with a $\lambda/4$ transmission-line resonator via a Josephson junction inserted at the end of a central conductor. By modulating an external flux through the superconducting quantum interference device (SQUID) loop of the transmon qubit, a desired sinusoidally modulated coupling can be obtained. However, the qubit transition frequency is also perturbed by a time-dependent control flux (with a frequency range about tens of MHz), which should be avoided in certain cases.

Here we demonstrate another possible hybrid circuit layout to realize such modulated interactions between high-frequency NAMR and superconducting qubits.

A. Flux-mediated coupling between SQUID and NAMR

We start our discussions by describing the interaction between a SQUID and a NAMR. As shown in Fig. 1, two Josephson junctions, each shunted by a capacitance C, are connected by a loop in the x-y plane. The total charging energy for two junctions is $E_c = e^2/C$. The NAMR with length l is coated with a superconductor and fabricated into the loop [61–63]. Alternatively, carbon nanotubes could be employed (acting as superconducting junctions *in situ*) to produce mechanical vibrations [47,64]. The NAMR (with mass m and frequency ω_m) vibrates along the z direction, and a
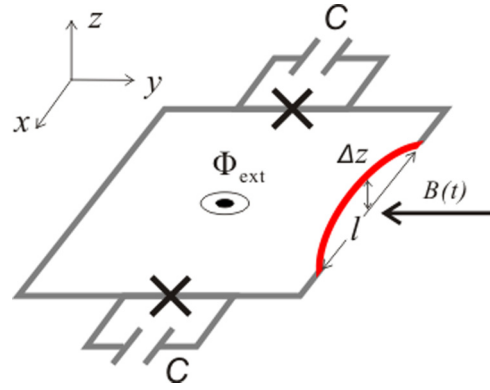

FIG. 1. Two Josephson junctions with an identical capacitance C form a SQUID loop in the x-y plane. A NAMR (represented by the red bow-shaped curve), with length l and mass m, is embedded in the loop and vibrates in the z direction with amplitude Δz. The static magnetic field perpendicular to the x-y plane produces a static flux Φ_{ext} for the SQUID. Additionally, there is a time-dependent magnetic field $B(t)$ (parallel to the x-y plane) applied to the loop area produced by the NAMR. The total flux through the SQUID is modulated by the vibrational motions of NAMR.

time-dependent magnetic field $B(t)$ is perpendicularly applied to the arm of the NAMR in the y direction [61,62].

Denoting the gauge-invariant phase difference by ϕ_i and the Josephson energy by E_{Ji} for the ith junction, we can write the total Josephson energy for the SQUID as ($\hbar = 1$)

$$
\begin{aligned}
E_J &= E_{J1} \cos \phi_1 + E_{J2} \cos \phi_2 \\
&= E_{J\Sigma}(\cos \phi_+ \cos \phi_- - d_0 \sin \phi_+ \sin \phi_-),
\end{aligned} \quad (1)
$$

where $E_{J\Sigma} = E_{J1} + E_{J2}$ is the total Josephson energy, $d_0 = (E_{J1} - E_{J2})/E_{J\Sigma}$ is the junction asymmetry, and $\phi_+ = (\phi_1 + \phi_2)/2$ represents the overall phase of the SQUID [64]. Note that $\phi_- = (\phi_1 - \phi_2)/2 = \pi \Phi_x/\Phi_0$ is bound by the fluxoid quantization relation, where Φ_x is the flux through the SQUID ring and Φ_0 is the flux quantum. Here we have neglected the geometric and kinetic inductances of the loop [65]. As shown in Fig. 1, there are two components for the flux Φ_x [47,66]: the static part Φ_{ext}, which is induced by a homogeneous magnetic field in the z direction, and a time-dependent part resulting from the NAMR vibrating around its equilibrium position and the y-direction magnetic field $B(t)$. Therefore, ϕ_- is expressed as

$$
\phi_- = \frac{\pi \Phi_x}{\Phi_0} = \frac{\pi}{\Phi_0}[\Phi_{\text{ext}} + B(t)\xi l \Delta z], \quad (2)
$$

where ξ is the average geometric constant [67] and Δz is the displacement of the NAMR away from its equilibrium position at $z = 0$.

Note that Φ_{ext} and $B(t)$ are induced by two magnetic fields with perpendicular directions. The first and second terms in Eq. (2) can, in principle, be changed independently. An imperfect perpendicular relation between these two magnetic fields might cause the net control flux, which should be minimized in experiments. To obtain the coupling relation between the vibration mode and the SQUID, we rewrite Eq. (1) as
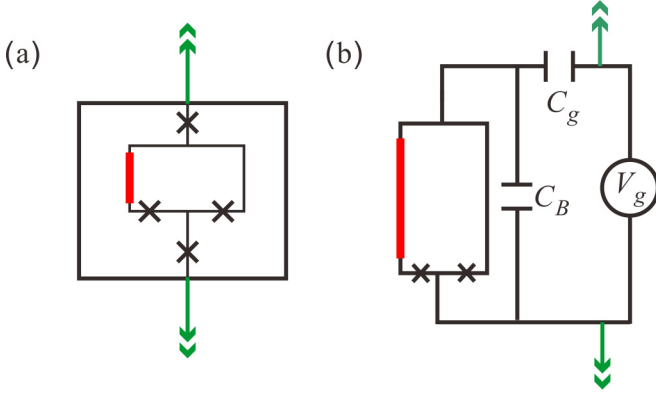
$$
E_J = E'_{J\Sigma} \cos(\phi_+ + \phi_0), \quad (3)
$$

FIG. 2. (a) Schematic diagram for coupling a NAMR with a flux qubit. The small α junction for the flux qubit is replaced by the SQUID in Fig. 1. The NAMR (the red thick line) vibrates in the direction perpendicular to this plane. (b) Schematic diagram of a NAMR coupled to a transmon qubit. Similar to the flux qubit case (a), the single junction is replaced by the hybrid mechanical-SQUID system. The time-dependent flux changes the effective Josephson energy of the transmon qubit. In panels (a) and (b), the coherent driving fields are applied through the 1D transmission line (green arrows).

where $E'_{J\Sigma} = E_{J\Sigma}\sqrt{\cos^2 \phi_- + d_0^2 \sin^2 \phi_-}$ is the effective Josephson energy and $\phi_0 = \arctan(d_0 \tan \phi_-)$ is the shifted phase. We assume that the junction asymmetry $d_0 \ll 1$ and ϕ_- is far away from $\pi/2$. As a result, ϕ_0 is only a small constant phase factor, which has a small effect on the kinetic energy [47]. The vibrational motion of the NAMR induces a flux perturbation on $E'_{J\Sigma}$. By expanding the displacement-dependent $E'_{J\Sigma}$ to the first order in Δz, we obtain

$$\frac{\partial E'_{J\Sigma}}{\partial \Delta z} = \frac{\partial E'_{J\Sigma}}{\partial \phi_-} \frac{\partial \phi_-}{\partial \Delta z}$$
$$= -\frac{\pi E_{J\Sigma} \sin(2\phi_-)(1 - d_0^2) B(t)\xi l}{2\Phi_0 \sqrt{(1 - d_0^2)\cos^2 \phi_- + d_0^2}}. \quad (4)$$

Considering that two junctions are symmetric with $d_0 = 0$, we reduce Eq. (4) to a simpler form

$$\frac{\partial E'_{J\Sigma}}{\partial \Delta z}\bigg|_{d_0=0} = -\frac{\pi E_{J\Sigma} \sin(\phi_-) B(t)\xi l}{\Phi_0}, \quad (5)$$

from which we find that the magnetic field $B(t)$, together with the mechanical oscillations, induce a time-dependent modulation of the effective Josephson energy $E'_{J\Sigma}$ of the SQUID.

B. Longitudinal interaction between superconducting qubits and NAMRs

In typical circuit layouts of a superconducting qubit, we often replace a nonlinear Josephson junction with a SQUID for tuning the Josephson energy, which enables more flexibility and tunability for controlling qubits. For example, as shown in Fig. 2(a), we consider a gradiometric gap-tunable flux qubit, where the SQUID and two identical junctions with their Josephson energy E_{J0} form two symmetric gradiometric loops

[68–71]. Compared with a three-junction flux qubit [72,73], the small α junction is replaced by a mechanical-SQUID system, where $\alpha = E'_{J\Sigma}/E_{J0}$ is operated in the regime $0.5 < \alpha < 1$ [65,69,73]. The NAMR is shown by the red thick line. As demonstrated in Refs. [68,70], around the optimal point, the Hamiltonian for the flux qubit can be approximately expressed as

$$H_q = \tfrac{1}{2}\Delta_t \sigma_z + \tfrac{1}{2}\epsilon \sigma_x, \quad (6)$$

where $\sigma_z = |e\rangle\langle e| - |g\rangle\langle g|$ and $\sigma_x = |e\rangle\langle g| + |g\rangle\langle e|$ are Pauli operators, given in terms of the ground $|g\rangle$ and excited $|e\rangle$ states of the qubit. Moreover, the energy bias $\epsilon = 2I_p \delta\Phi_q$ is controlled via the imbalance flux $\delta\Phi_q$ through the two gradiometric loops and I_p is the persistent-current amplitude. In experiments, $\delta\Phi_q$ can be induced via a propagating microwave field in a 1D transmission line [green line in Fig. 2(a)].

The energy gap Δ_t depends on the parameter α. Specifically, the following approximate analytical expression can be obtained by tight-binding calculations of the eigenstates [65,73]:

$$\Delta_t = \sqrt{\frac{4E_{J0}E_C(2\alpha^2 - 1)}{\alpha}}$$
$$\times \exp\left[-g(\alpha)\sqrt{4\alpha(1 + 2\alpha)\frac{E_J}{E_C}}\right], \quad (7)$$

where $g(\alpha) = \sqrt{1 - 1/(4\alpha^2)} - \arccos[1/(2\alpha)]/(2\alpha)$. Note that α linearly depends on the effective Josephson energy $E'_{J\Sigma}$ of the SQUID. Therefore, we can express the sensitivity R_f of the gap Δ_t to the flux control ϕ_- through the SQUID loop as follows [65,69]:

$$R_f = \frac{\partial \Delta_t}{\partial \phi_-} = \frac{\partial \Delta_t}{\partial \alpha}\frac{\partial \alpha}{\partial E'_{J\Sigma}}\frac{\partial E'_{J\Sigma}}{\partial \phi_-}, \quad (8)$$

where $\partial \Delta_t/\partial\alpha$ is obtained from Eq. (7) and $\partial E'_{J\Sigma}/\partial\phi_-$ is given in Eq. (4). Indeed, the flux sensitivity R_f could be directly obtained in experiments by detecting a qubit spectrum via sweeping the flux control ϕ_-. As shown in Refs. [68,69], R_f is about 0.07–0.7 GHz/mΦ_0. The flux perturbation results from the vibrations of the NAMR and the time-dependent magnetic field $B(t)$ [74] and, therefore, Δ_t can be approximately rewritten as

$$\Delta_t = \Delta_t(z = 0) + R_f \frac{\partial \phi_-}{\partial \Delta z}\Delta z$$
$$= \Delta_t(z = 0) + R_f \frac{\pi B(t)\xi l}{\Phi_0}\Delta z, \quad (9)$$

where $\Delta_t(z = 0)$ is the energy gap of the qubit when the NAMR is at its equilibrium position $z = 0$.

Following Eqs. (6)–(9) and considering the NAMR free energy, the Hamiltonian of this hybrid system becomes

$$H_c = \tfrac{1}{2}\Delta_t(z = 0)\sigma_z + \tfrac{1}{2}\epsilon\sigma_x + \omega_m b^\dagger b + g(t)\sigma_z(b^\dagger + b), \quad (10)$$

where b ($b^\dagger$) is the phonon annihilation (creation) operator of the NAMR. By expanding $B(t)$ with its Fourier transform of frequency ω', the longitudinal-interaction strength can be written as

$$g(t) = R_f \frac{\pi\xi l}{\Phi_0} x_0 \sum_{\omega'}[B(\omega')e^{-i\omega' t} + B^\star(\omega')e^{i\omega' t}], \quad (11)$$

where $x_0 = \sqrt{1/(2m\omega_m)}$ is the zero-point fluctuation of the NAMR and $|B(\omega')|$ is the magnetic-field amplitude of the frequency ω' component. However, the magnetic noise through the SQUID loop also causes decoherence of the qubit via the flux sensitivity R_f *in situ* [65,68,69]; the relaxation times (both T_1 and T_2) decrease with increasing R_f. To suppress these decoherence processes, we should control R_f below a certain level.

Besides employing a flux qubit, it is possible to induce the time-dependent interaction between a transmon qubit [75–78] and a NAMR. As depicted in Fig. 2(b), the single Josephson junction for the transmon qubit is replaced by a SQUID embedded by a NAMR. The charging energy E_C is reduced by adding a large shunt capacitance C_B [75–77], and the transmon qubit is insensitive to charge noise under the condition $E'_{J\Sigma} \gg E_C$. For simplicity, we assume that the driving field propagating along the 1D transmission line (plotted as green arrows in Fig. 2) and the bias voltage V_g are applied to the gate capacitance C_g. Given that the transmon qubit, shown in Fig. 2(b), can be approximately viewed as a Duffing oscillator, the transition frequency between the two lowest eigenstates is [64,75]

$$E_{01} = \sqrt{8E_C E'_{J\Sigma}} - E_C. \quad (12)$$

For simplicity, we consider the symmetric junction at $d_0 = 0$; then the flux sensitivity on E_{01} of the transmon qubit is

$$R_t = \frac{\partial E_{01}}{\partial \phi_-} = \frac{\partial E_{01}}{\partial E'_{J\Sigma}} \frac{\partial E'_{J\Sigma}}{\partial \phi_-}$$
$$= \sqrt{2E_C E_{J\Sigma}} \sin\phi_- \tan\phi_-. \quad (13)$$

By assuming that $E_{J\Sigma} = 70$ GHz, $E_C = 2$ GHz, and $\phi_- = \pi/3$, we obtain $R_t \simeq 0.064$ GHz/mΦ_0. Similar to the above discussions about our derivation of Eq. (12), we can also obtain the modulated coupling between the transmon qubit and the NAMR.

Here we discuss the coupling strength under current experimental conditions, and choose a carbon-nanotube resonator as the NAMR, e.g., with effective mass $m = 4 \times 10^{-21}$ kg and fundamental frequency $\omega_m/(2\pi) = 100$ MHz [79–82]. The NAMR length can be of 3 μm with geometric constant $\xi = 0.9$ [47,61,67]. Employing the flux sensitivity $R_{f,t} = 0.25$ GHz/mΦ_0 and the magnetic-field amplitude $|B(\omega')| \simeq 800$ μT, the coupling strength for the frequency component ω' is about $g(\omega')/(2\pi) \simeq 8$ MHz.

There are many potential applications for these time-dependent longitudinally coupled systems, such as generating macroscopic nonclassical states and performing quantum non-demolition measurements of the qubit states [43,44].

In the following, we discuss the optical response of a microwave field applied to the qubit, and show how to observe various types of tunable EIT based on such a hybrid system.

III. EFFECTIVE HAMILTONIAN FOR TUNABLE SIDEBAND TRANSITIONS

To observe sideband transitions and EIT, we assume that a strong drive and a weak probe, with frequencies ω_{drv} and ω_{pr}, respectively, are applied to the superconducting qubit through the 1D transmission line [55,83–85]. The coherent drive and probe fields are both approximately at the qubit transition frequency ω_q, which is usually around several GHz. Therefore, the oscillation frequency of the counter-rotating terms is about $2\omega_q$. In the following discussions, the Rabi frequencies of the drive and probe fields are assumed to be within several MHz. Therefore, we can adopt the rotating wave approximation and neglect the counter-rotating terms. Thus the driven hybrid system can be written as

$$\bar{H} = \frac{1}{2}\omega_q\sigma_z + \omega_m b^\dagger b + g(t)\sigma_z(b + b^\dagger)$$
$$- [(\Omega_{\mathrm{drv}}e^{-i\omega_{\mathrm{drv}}t} + \Omega_{\mathrm{pr}}e^{-i\omega_{\mathrm{pr}}t})\sigma_+ + \mathrm{H.c.}], \quad (14)$$

where Ω_{drv} and Ω_{pr} are the Rabi frequencies of the drive and probe fields, respectively, and $\sigma_+ = |e\rangle\langle g|$ ($\sigma_- = |g\rangle\langle e|$) is the raising (lowering) operator for the qubit.

Applying a frame rotating at frequency ω_{drv}, the Hamiltonian in Eq. (14) is transformed to

$$\bar{H} = \frac{1}{2}\Delta_0\sigma_z + \omega_m b^\dagger b + g(t)\sigma_z(b + b^\dagger)$$
$$- \Omega_{\mathrm{drv}}(\sigma_+ + \sigma_-) - \Omega_{\mathrm{pr}}(\sigma_+ e^{-i\delta t} + \sigma_- e^{i\delta t}), \quad (15)$$

where $\Delta_0 = \omega_q - \omega_{\mathrm{drv}}$ is the qubit-drive detuning, $\delta = \omega_{\mathrm{pr}} - \omega_{\mathrm{drv}}$ is the probe-drive detuning, and $\sigma_x = \sigma_+ + \sigma_-$. Assuming that $\Omega_{\mathrm{drv}} \gg \Omega_{\mathrm{pr}}$, we can neglect the last term in Eq. (15). By applying the time-dependent polariton transformation $U(t) = \exp[\sigma_z Y(t)]$ to $\bar{H}$ (see, e.g., [44]), where $Y(t) = \beta^*(t)b^\dagger - \beta(t)b$, we obtain the transformed Hamiltonian

$$H = U^\dagger(t)\bar{H}U(t) - iU^\dagger(t)\frac{\partial U(t)}{\partial t}$$
$$= \frac{1}{2}\Delta_0\sigma_z + \omega_m b^\dagger b + \sigma_z[\eta(t)b + \eta^*(t)b^\dagger]$$
$$- \Omega_{\mathrm{drv}}[\sigma_+ e^{2Y(t)} + \mathrm{H.c.}], \quad (16)$$

where $\eta(t) = g(t) - \omega_m\beta(t) + i\frac{\partial}{\partial t}\beta(t)$. We can eliminate the longitudinal-coupling terms in Eq. (16) by setting $\eta(t) \equiv 0$. Assuming that $\beta(t) = M(t) + iN(t)$, the following relations should be satisfied:

$$0 = -\omega_m M(t) + g(t) - \frac{\partial N(t)}{\partial t}, \quad (17)$$

$$0 = -\omega_m N(t) + \frac{\partial M(t)}{\partial t}. \quad (18)$$

To simplify our analysis, we assume that $g(t)$ is sinusoidally modulated by a monochromatic drive at frequency ω_g, i.e.,

$$g(t) = g_0\cos(\omega_g t). \quad (19)$$

The general solution for the differential Eqs. (17) and (18) has the form

$$\beta(t) = C_0 e^{-i\omega_m t} + \frac{g_0}{\omega_m^2 - \omega_g^2}[\omega_m\cos(\omega_g t) - i\omega_g\sin(\omega_g t)], \quad (20)$$

where C_0 is an arbitrary complex coefficient. For simplicity, by setting $C_0 = 0$, $\beta(t)$ is reduced to

$$\beta(t) = \frac{g_0}{2}\left(\frac{e^{i\omega_g t}}{\omega_m + \omega_g} + \frac{e^{-i\omega_g t}}{\omega_m - \omega_g}\right). \quad (21)$$

Under the condition $\eta(t) = 0$, Eq. (16) is simplified as

$$H = \frac{1}{2}\Delta_0\sigma_z + \omega_m b^\dagger b - \Omega_{\mathrm{drv}}[\sigma_+ e^{2Y(t)} + \mathrm{H.c.}]. \quad (22)$$

The coupling-modulation frequency ω_g and the coupling constant g_0 are assumed to be much smaller than the NAMR frequency, i.e., $\{\omega_g, g_0\} \ll \omega_m$. Therefore, $|\beta(t)|$ is always a small dimensionless parameter, as it holds

$$|\beta(t)| \leqslant \frac{g_0 \sqrt{\omega_m^2 + \omega_g^2}}{\omega_m^2 - \omega_g^2} \ll 1. \quad (23)$$

Expanding the last term of Eq. (22) to the third order in $\beta(t)$, the Hamiltonian reads

$$H = \tfrac{1}{2}\Delta_0 \sigma_z + \omega_m b^\dagger b - \Omega_{\mathrm{drv}}[\sigma_+ + \sigma_-]$$
$$- 2\Omega_{\mathrm{drv}}\left\{\sigma_+\left[Y(t) + Y^2(t) + \tfrac{2}{3}Y^3(t)\right] + \mathrm{H.c.}\right\}. \quad (24)$$

We assume a red-sideband drive field with an amplitude, which is weak compared with the detuning frequency, i.e., $\Omega_{\mathrm{drv}} \ll \Delta_0 \simeq \omega_m$. Similar to discussions in Ref. [86], the third term in Eq. (24) leads to a dynamical Stark shift for the qubit. We can rewrite the Hamiltonian in Eq. (24) in the basis of its eigenstates:

$$|+\rangle = \cos\frac{\theta}{2}|e\rangle + \sin\frac{\theta}{2}|g\rangle, \quad (25a)$$

$$|-\rangle = \cos\frac{\theta}{2}|g\rangle - \sin\frac{\theta}{2}|e\rangle, \quad (25b)$$

with $\tan\theta = -2\Omega_{\mathrm{drv}}/\Delta_0$. Since $\theta \ll 1$, we can neglect the rotating angle of the qubit basis. The dynamical Stark shift slightly shifts the qubit-transition frequency. Thus we should replace the detuning Δ_0 in the qubit free-energy term in Eq. (24) with a modified qubit-drive detuning

$$\widetilde{\Delta} = \sqrt{\Delta_0^2 + 4\Omega_{\mathrm{drv}}^2}. \quad (26)$$

We assume that the drive detuning $\delta_s \equiv \widetilde{\Delta} - \omega_m$ is of the same order as coupling-modulation frequency ω_g. According to Eq. (23), $|\beta(t)|$ is a small parameter and it can easily be verified that $|\beta(t)|^N \Omega_{\mathrm{drv}} \ll \omega_m \simeq \widetilde{\Delta}$ ($N = 1, 2, 3$). Under these conditions, we can neglect the rapidly oscillating terms in Eq. (24). By applying the unitary transformation $U_0(t) = \exp[-i(\widetilde{\Delta}\sigma_z + \omega_m b^\dagger b)t]$ to Eq. (24), we obtain the effective Hamiltonian

$$H = \xi(t)\sigma_+ b \exp(i\delta_s t) + \mathrm{H.c.} \quad (27)$$

Note that $\xi(t)$ has been decomposed into the frequency components $\pm\omega_g$ and $\pm 3\omega_g$ as follows:

$$\xi(t) = 2\beta(t)\Omega_{\mathrm{drv}} - \frac{4N}{3}\beta(t)^2\beta^*(t)\Omega_{\mathrm{drv}}$$
$$= \sum_{j=\pm}(C_{1j}e^{ji\omega_g t} + C_{3j}e^{j3i\omega_g t}), \quad (28)$$

with the first- and third-order sideband transition rates given respectively by

$$C_{1\pm} = \frac{g_0\Omega_{\mathrm{drv}}}{\omega_m \mp \omega_g} - \frac{4Ng_0^3\Omega_{\mathrm{drv}}(3\omega_m \mp \omega_g)}{3(\omega_m^2 - \omega_g^2)^2}, \quad (29)$$

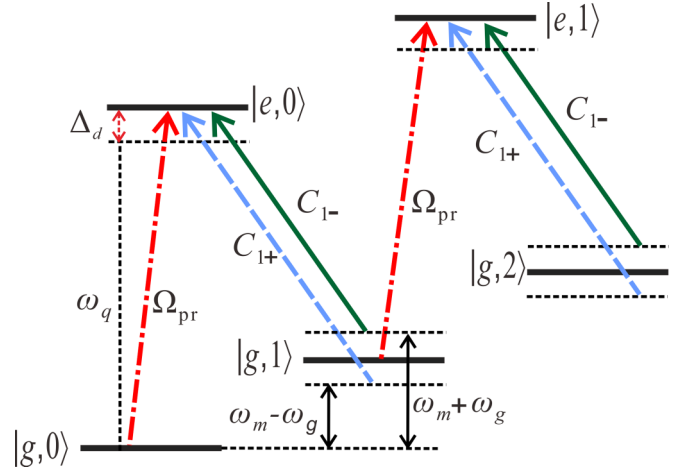$$C_{3\pm} = \frac{4Ng_0^3\Omega_{\mathrm{drv}}}{3(\omega_m^2 - \omega_g^2)(\omega_m \mp \omega_g)}, \quad (30)$$

FIG. 3. Lowest-energy levels of the qubit-NAMR system and possible state transitions induced by a sideband drive (of frequency Ω_{drv}, which is not shown here) and a resonant probe (of frequency Ω_{pr}, represented by the red dashed-dotted arrow). The dynamical Stark shift Δ_d results from the detuning of the drive field. Due to a sinusoidal modulation of the longitudinal coupling at frequency ω_g, the first-order sideband transition, induced by the drive field (from $|e, n\rangle$ to $|g, n+1\rangle$), is split into two transitions with rates C_{1+} (blue dashed arrows) and C_{1-} (green solid arrows). Note that ω_q (ω_m) is the qubit (NAMR) frequency and ω_g is the coupling-modulation frequency.

where $N = \langle b^\dagger b\rangle - 1$ with $\langle b^\dagger b\rangle$ being the average phonon number. The NAMR is assumed to be in the quantum regime with several phonons, and N is not large. When deriving Eq. (27), the rapidly oscillating terms were neglected and only near-resonant ones were kept. Equation (24) was expanded to third order in $Y(t)$ only, as observable effects of higher-order terms can be ignored. If sweeping the sideband drive frequency around the regime $\widetilde{\Delta} \simeq \omega_m$, four apparent resonant positions can be observed at $\delta_s = \pm\omega_g, \pm 3\omega_g$. It is easy to find first-order transition rates

$$C_{1\pm} \simeq \frac{g_0\Omega_{\mathrm{drv}}}{\omega_m \mp \omega_g} \gg C_{3\pm} \quad (31)$$

by assuming that $|\beta(t)| \ll 1$. In some of the following discussions, we neglect the third-order transition rates $C_{3\pm}$. To observe the optical response of the probe field, the probe term should be added (in the rotating frame); then the total Hamiltonian becomes

$$H = \sum_{j=\pm}[C_{1j}\sigma_+ b\, e^{i(j\omega_g + \delta_s)t} - \Omega_{\mathrm{pr}}\sigma_+ e^{i(\widetilde{\Delta}-\delta)t}] + \mathrm{H.c.} \quad (32)$$

The energy-level diagram is depicted in Fig. 3. Due to the sinusoidal modulation of the longitudinal coupling, the monochromatic drive field with strength Ω_{drv} in the original Hamiltonian, given by Eq. (14), induces two coherent transition processes between the states $|g, n+1\rangle \leftrightarrow |e, n\rangle$. The corresponding transition rates are $C_{1\pm}$ (as shown with blue dashed and green solid arrows). After compensating the dynamical Stark shift $\Delta_d = \omega_q - \omega_{\mathrm{pr}}$, the frequency separation between these two coherent transitions is equal to the doubled coupling-modulation frequency, i.e., $2\omega_g$. In the following discussions, we will show that, assuming that the drive field is tuned

properly, both conventional and bichromatic EIT (or two-color EIT) can be observed in such a hybrid system.

IV. ELECTROMAGNETICALLY INDUCED TRANSPARENCY

In this section, we discuss the optical response to the probe field via the standard master equation approach in our proposal. The Born-Markov approximation is valid here. Therefore, the system evolution is approximately described by the Lindblad-type master equation

$$\frac{d\rho(t)}{dt} = -i[H, \rho(t)] + \Gamma_d D[\sigma_-]\rho(t) + \Gamma_\phi D[\sigma_z]\rho(t)$$
$$+ (n_{\text{th}} + 1)\kappa D[b]\rho(t) + n_{\text{th}}\kappa D[b^\dagger]\rho(t), \quad (33)$$

where $D[A]\rho = (2A\rho A^\dagger - A^\dagger A\rho - \rho A^\dagger A)/2$ are the decoherence terms of the Lindblad superoperator form, Γ_d (Γ_ϕ) is the decay (pure dephasing) rate of the qubit, and κ is the relaxation rate of the mechanical mode due to its coupling with a finite-temperature environment with a mean thermal phonon number n_{th}. Employing the methods of Refs. [55,83,85,87], one can approximately assume that the decay of the qubit is caused only by the quantum noise in a 1D open line. The coherent drive and probe fields for the qubit are also applied through the 1D transmission line. Since the size of the qubit loop ($\sim\mu$m) is much smaller than the wavelength of the microwave drive ($\sim$cm), we assume that the drive is place independent [83].

The time-dependent atomic dipole moments can be expanded in terms of the frequency Fourier components as [50]

$$\langle\sigma_-(\omega')\rangle = \sum_{\omega'=-\infty}^{\omega'=\infty} \langle\sigma_-(t)\rangle \exp(-i\omega't), \quad (34)$$

where $\langle\sigma_+(t)\rangle$ can be found by numerically solving the master equation (33). Different from employing a susceptibility to describe the optical response of an atomic ensemble [27,88], here we should use the reflection coefficient $r(\omega_{\text{pr}})$ to characterize the electromagnetic response for the probe field of a single atom [74], which can be obtained via the following relation [83,87]:

$$r(\omega_{\text{pr}}) = -\frac{i\Gamma_d\langle\sigma_-(\omega_{\text{pr}})\rangle}{2\Omega_{\text{pr}}}. \quad (35)$$

The real $\text{Re}[r(\omega_{\text{pr}})]$ and imaginary $\text{Im}[r(\omega_{\text{pr}})]$ parts of the reflection coefficient are related to the reflection and dispersion of a single atom, respectively. In the following, we discuss how $r(\omega_{\text{pr}})$ behaves under different drive and probe conditions.

A. Single-color EIT

The two split-sideband transitions are well separated under the condition $C_\pm \ll 2\omega_g$. Assuming that $\delta_s = -\omega_g$ ($\delta_s = \omega_g$), only the sideband transition C_{1+} (C_{1-}) is on resonance, and we reduce the Hamiltonian, in Eq. (32), by adopting the rotating wave approximation, as follows:

$$H_\pm = \{C_{1\pm}\sigma_+ b - \Omega_{\text{pr}}\sigma_+ \exp[i(\omega_m \mp \omega_g - \delta)t]\} + \text{H.c.} \quad (36)$$

Under these conditions, the dynamical Stark shifts of the qubit for the Hamiltonians $H_\pm$ are expressed as

$$\Delta_{d\pm} = \sqrt{(\omega_m \mp \omega_g)^2 - 4\Omega_{\text{drv}}^2} - (\omega_m \mp \omega_g)$$
$$\simeq \frac{2\Omega_{\text{drv}}^2}{\omega_m \mp \omega_g} \simeq \frac{2\Omega_{\text{drv}}^2}{\omega_m}. \quad (37)$$

To observe single-color EIT, we assume that the sideband transition C_{1+} is resonantly selected. Moreover, to suppress the transition C_{1-}, the condition $C_\pm \ll 2\omega_g$ should always be satisfied to ensure the validity of the rotating wave approximation. When the probe-drive detuning satisfies the condition $\delta = \omega_m - \omega_g$, as shown in Fig. 3, the transitions are represented by the red and blue arrows. As a result, the evolution of the system is approximately described by the time-independent Hamiltonian

$$H_+ = (C_{1+}\sigma_+ b - \Omega_{\text{pr}}\sigma_+) + \text{H.c.} \quad (38)$$

Assuming that the NAMR has a high-quality factor and the condition $\min\{C_{1+}, \omega_{\text{pr}}, \Gamma_d\} \gg n_{\text{th}}\kappa$ is satisfied, the decoherence process of the NAMR can be neglected. The effective Hamiltonian $H = H_+$, together with the rapid decay of the qubit, drives the system into the following dark state [86,89]:

$$|\Psi_{\text{ds}}\rangle = e^{-|\lambda^2|/2} \sum_n \frac{\lambda^n}{\sqrt{n!}} |g, n\rangle = |g\rangle|\alpha_\lambda\rangle, \quad (39)$$

where $\lambda = \Omega_{\text{pr}}/C_{1+}$ and $|\alpha_\lambda\rangle$ is a coherent state.

In a typical EIT system, the probe field is weak compared with the control field, i.e., $\Omega_{\text{pr}} \ll C_{1+}$. Therefore, $\lambda \ll 1$, and we can use the states $|g, 0\rangle$, $|g, 1\rangle$, and $|e, 0\rangle$ to describe the transitions governed by Eq. (36). The relation between these three states is similar to a Λ-type EIT system. The reflection coefficient of the probe field for $H = H_+$ in Eq. (36) is expressed as [27,88]

$$r_{\text{eff}}(\omega_{\text{pr}}) = \frac{\Gamma_d}{2\Gamma_f - 2i(\delta - \omega_m + \omega_g) + \frac{4C_{1+}^2}{\kappa - 2i(\delta - \omega_m + \omega_g)}}, \quad (40)$$

where $\Gamma_f = \Gamma_d/2 + 2\Gamma_\phi$ is the total dephasing rate. Equation (40) indicates that the mechanical decay rate κ determines the width of the EIT window. Thus very narrow EIT windows can be observed in our proposal by adopting a high quality-factor NAMR with $\Gamma_f \gg \kappa$. If the NAMR is implemented by a carbon nanotube, the quality factor can be extremely high [90]. Thus we assume that the NAMR is vibrating at mechanical frequency $\omega_m/(2\pi) = 100$ MHz with $\kappa/(2\pi) = 1$ KHz (see [81,82]). The Rabi frequencies of the two coherent drives are $\Omega_{\text{drv}}/(2\pi) = 10$ MHz and $\Omega_{\text{pr}}/(2\pi) = 0.2$ MHz, respectively. For the modulated coupling $g(t)$, we set $g_0/(2\pi) = 8$ MHz and $\omega_g/(2\pi) = 4$ MHz, as discussed in Sec. II B. According to Eq. (29), the effective sideband transition rate is $C_{1+}/(2\pi) = 0.8$ MHz. For a superconducting qubit interacting with an open one-dimensional transmission line, the energy relaxation and dephasing rates are about MHz [83,84], and here we set $\Gamma_d/(2\pi) = 3$ MHz and $\Gamma_\phi/(2\pi) = 0.2$ MHz, respectively. Employing these parameters, in Fig. 4(a) we plot $\text{Re}[r(\omega_{\text{pr}})]$ (red solid curve) and $\text{Im}[r(\omega_{\text{pr}})]$ (blue solid curve) changing with the detuning $(\delta - \omega_m + \omega_g)$ by numerically solving the master equation with the original Hamiltonian
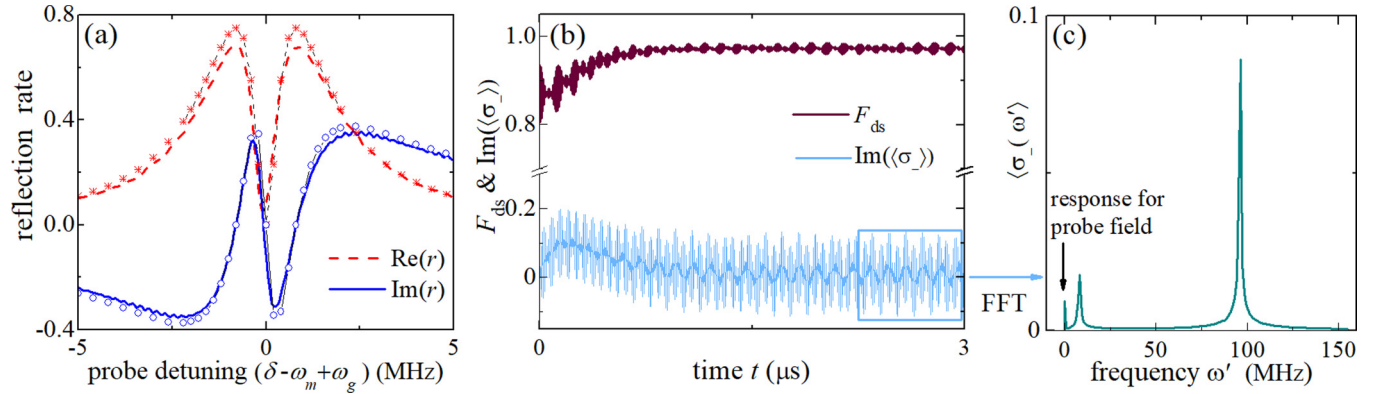
FIG. 4. Single-color EIT with $\delta_s = -\omega_g$. (a) The real and imaginary parts of the reflection coefficient r, $\mathrm{Re}(r)$ (red dashed curve) and $\mathrm{Im}(r)$ (blue solid curve), as functions of the drive-probe detuning $(\delta - \omega_m + \omega_g)$ based on our numerical simulation. The curves shown with stars and circles are plotted according to analytical Eq. (40). At $\delta = \omega_m - \omega_g$, $\mathrm{Re}(r)$ displays a dip with $\mathrm{Re}(r) \simeq 0$. (b) Time evolutions of the dark-state fidelity $F_{\mathrm{ds}}(t)$ (upper curves), given in Eq. (33), and $\mathrm{Im}\langle\sigma_-\rangle$ (lower curves) of the qubit for the dip position in (a). Note that $\mathrm{Im}\langle\sigma_-\rangle$ oscillates around zero. (c) Employing the fast Fourier transform (FFT), $\mathrm{Im}\langle\sigma_-\rangle$ in (b) is decomposed in the frequency domain. Since our numerical calculations are performed in the rotating frame of the probe field frequency, the dc (zero-frequency) component of $\mathrm{Im}\langle\sigma_-\rangle$ corresponds to the optical response of the probe field, which has a low amplitude with $\mathrm{Im}\langle\sigma_-(\omega'=0)\rangle \simeq 9 \times 10^{-3}$, when EIT occurs. The parameters are $\omega_m/(2\pi) = 100$ MHz, $\Omega_{\mathrm{drv}}/(2\pi) = 10$ MHz, $\Omega_{\mathrm{pr}}/(2\pi) = 0.2$ MHz, $g_0/(2\pi) = 8$ MHz, $\omega_g/(2\pi) = 4$ MHz, $\Gamma_d/(2\pi) = 3$ MHz, $\Gamma_\phi/(2\pi) = 0.25$ MHz, $n_{\mathrm{th}} = 0$, and $\kappa/(2\pi) = 1$ KHz.

in Eq. (15) (rotating at the probe frequency). Moreover, the analytical form for r_{eff}, given in Eq. (40), is also plotted with the curves shown with symbols.

In Fig. 4(a), one can see a single EIT dip with $\mathrm{Re}[r(\omega_{\mathrm{pr}})] \simeq 0$ around $\delta = \omega_m - \omega_g$. Different from conventional atomic EIT, the control field here is not a semiclassical coherent drive, but a parametrically modulated coupling inducing a sideband transition C_{1+}. Moreover, we find that our analytical and numerical results of the optical response match well with each other, indicating that the Hamiltonian Eq. (38) can effectively describe the transition relation of the single-window EIT in Fig. 4(a).

Defining the fidelity

$$F_{\mathrm{ds}}(t) = \langle\Psi_{\mathrm{ds}}|\rho(t)|\Psi_{\mathrm{ds}}\rangle \tag{41}$$

for the dark state in Eq. (39), Fig. 4(b) depicts the time evolution of this fidelity and $\mathrm{Im}\langle\sigma_-(t)\rangle$ with $\delta = \omega_m - \omega_g$ [the dip position in Fig. 4(a)]. The numerical results clearly show that the system is rapidly steered into its dark state with the steady fidelity $F_{\mathrm{ds}} \simeq 98.5\%$. Note that $\mathrm{Im}\langle\sigma_-(t)\rangle$ oscillates in time, and it contains many frequency components. The fast Fourier transform of $\mathrm{Im}\langle\sigma_-(t)\rangle$ is shown in Fig. 4(c), which exhibits three main peaks in the low-frequency regime. The first peak at $\omega' = 0$ (i.e., the dc component) corresponds to the optical response of the probe field. This peak has very low amplitude due to EIT.

Note that the NAMR has much lower eigenfrequency than that of the qubit, so it might couple with a finite-temperature environment with thermal phonon number n_{th}. Once the effective decay rate $n_{\mathrm{th}}\kappa$ of the NAMR is close to $\min\{C_{1+}, \omega_{\mathrm{pr}}, \Gamma_d\}$, the dark state, given in Eq. (39), is destroyed by thermal noise. In Fig. 5, we show how the reflection rate behaves around the EIT window for different values of n_{th}. We find that, when increasing n_{th}, the EIT dip becomes shallower with a wider EIT window, indicating that EIT is influenced by thermal phonons. However, only when n_{th} is $\geqslant 300$, this damage effect is clearly

apparent. For the case with $n_{\mathrm{th}} = 30$, the EIT effect differs only slightly from the zero-temperature case ($n_{\mathrm{th}} = 0$). Given that the proposed system is placed in a dilution refrigerator at 20 mK, the corresponding thermal phonon occupation is $n_{\mathrm{th}} \simeq 4$ and the EIT condition $\min\{C_{1+}, \omega_{\mathrm{pr}}, \Gamma_d\} \gg n_{\mathrm{th}}\kappa$ can be easily satisfied. Therefore, the thermal noise affecting the NAMR can be neglected in our discussions.

The single-color EIT demonstrated here is quite different from the case when the qubit-NAMR longitudinal coupling is constant [86,91], where the drive-probe detuning should be fixed and exactly equal to the eigenfrequency of the NAMR. In the case studied here with a modulation interaction, the drive-probe detuning is continuously changed by varying the coupling-modulation frequency ω_g, which is analogous to
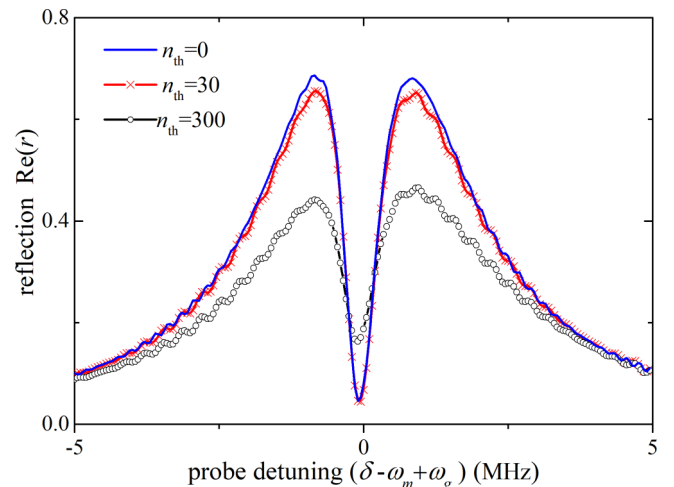

FIG. 5. Real part of the reflection coefficient r, $\mathrm{Re}(r)$, as a function of the probe detuning $(\delta - \omega_m + \omega_g)$ for $n_{\mathrm{th}} = 0$ (blue solid curve), $n_{\mathrm{th}} = 30$ (red cross), and $n_{\mathrm{th}} = 300$ (black circle). Other parameters employed here are the same as those in Fig. 4.
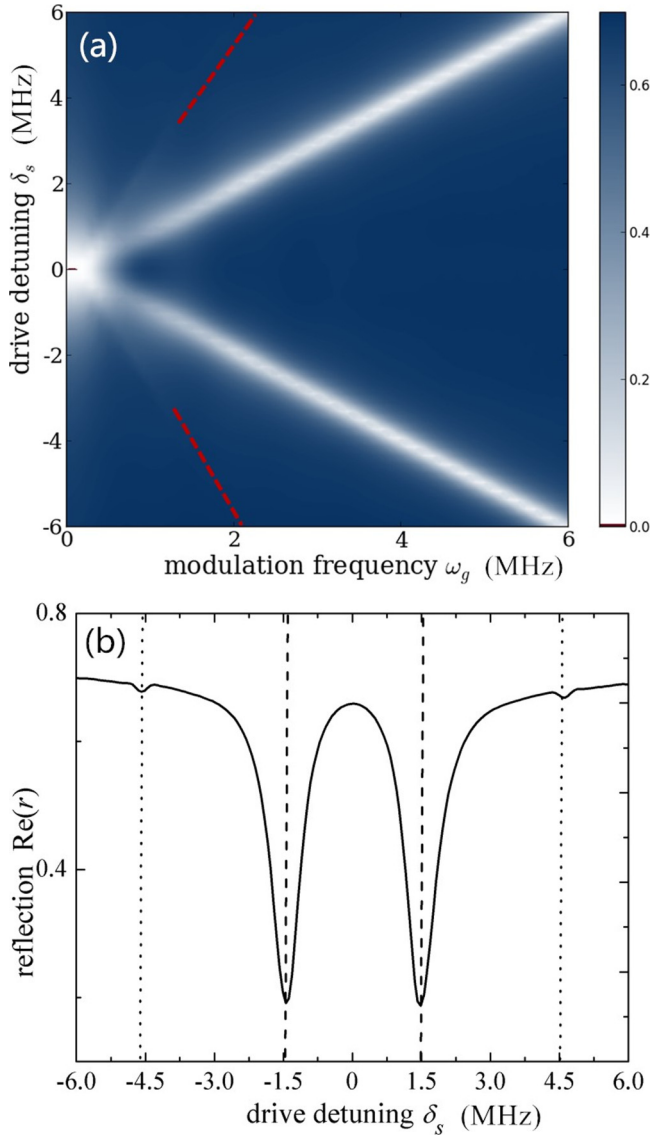
FIG. 6. (a) Reflection rate Re(r) of the resonant probe field versus the drive detuning δ_s and the coupling-modulation frequency ω_g. At $\omega_g = 0$, there is only one sideband drive frequency for the single-color EIT window. With increasing ω_g, the single dip for the EIT drive field is split into two apparent dips at $\delta_s \simeq \pm\omega_g$, and two less apparent dips at $\delta_s \simeq \pm3\omega_g$ as additionally indicated by the dotted red lines. (b) The cross section of figure (a) at $\omega_g/(2\pi) = 1.5$ MHz. Two shallow dips induced by the third-order terms $C_{3\pm}$ can be observed at $\delta_s/(2\pi) = \pm4.5$ MHz. Other parameters employed here are the same as those in Fig. 4.

changing the frequency difference between two metastable states in an EIT system. This can be clearly seen in Fig. 6(a), where we fix the probe field to be resonantly applied to the qubit, and plot the optical response Re[$r(\omega_{pr})$] by changing the drive detuning δ_s and the coupling-modulation frequency ω_g. At $\omega_g \simeq 0$, there is only one drive-probe detuning position for the single EIT window ($\tilde{\Delta} \simeq \omega_m$). Intriguingly, when we start to increase the frequency ω_g from zero, the single dip of the reflection rate as a function of the drive detuning splits into two apparent dips separated by $2\omega_g$, which corresponds to the

transition rates C_{1+} and C_{1-}, respectively. Two possible drive frequencies can induce single-color EIT. Thus modulating the qubit-NAMR coupling at frequency ω_g is equivalent to replacing the single NAMR with two frequency tunable NAMRs with frequencies $\omega'_m = \omega_m \pm \omega_g$.

Moreover, we find *two shallow dips* along the dashed lines in Fig. 6(a), which can be seen clearly in the cross-section plot Fig. 6(b) by fixing the coupling-modulation frequency at $\omega_g/(2\pi) = 1.5$ MHz. The relation between drive detuning and the modulation frequency is approximately given by $\delta_s \simeq \pm3\omega_g$. These two transparent dips result from the third-order resonant couplings $C_{3\pm}$ in Eq. (30). However, due to extremely low rates, these two dips are much shallower than those induced by $C_{1\pm}$.

B. Two-color EIT

In previous discussions, we found that only one sideband transition was dominant by setting the coupling-modulation frequency $\delta_s = \pm\omega_g$. However, by assuming that $\delta_s = 0$, the two sideband transitions (with strengths $C_{\pm}$) correspond to the same detuning, so both of these should be considered equally. The Hamiltonian in Eq. (32) is now reduced to

$$H = \sum_{j=\pm}[C_{1j}\sigma_+ b\, e^{ji\omega_g t} - \Omega_{pr}\sigma_+ e^{i(\omega_m-\delta)t}] + \text{H.c.} \quad (42)$$

As shown in Fig. 3, both sideband transitions C_{1+} and C_{1-} are detuned by ω_g. The energy-level transition relation is similar to two-color EIT with two control fields studied in Refs. [50–52]. Two transparent windows for the probe field were observed. In contrast to two-color EIT studies in atomic systems [48,50,52,92], only one (not two) coherent drive is employed here. The two split transparent windows result from a monochromatic modulation of the longitudinal coupling. Indeed, if $g(t)$ contains N well-separated frequency components, $2N$ windows of EIT can be observed.

Analogous to a conventional Λ-type EIT system, if we consider only one detuning sideband transition (either C_{1-} or C_{1+}) of detuning ω_g in Eq. (42), the reflection coefficient becomes

$$r_{\text{eff}\pm}(\omega_{pr}) = \frac{\Gamma_d}{2\Gamma_f - 2i(\delta - \omega_m) + \frac{4C_{1\pm}^2}{\kappa - 2i(\delta - \omega_m \mp \omega_g)}}, \quad (43)$$

with a real part, which has dip positions at $\delta - \omega_m = \pm\omega_g$. If both sideband transitions C_{1-} and C_{1+} occur with a symmetric detuning, the optical response for the probe field should combine these two EIT effects.

In Fig. 7, the imaginary and real parts of the reflection coefficient $r(\omega_{pr})$ are plotted based on our numerical simulations (the blue solid and red dashed curves). Around $\delta - \omega_m \simeq \pm\omega_g$, the two EIT windows emerge with typical anomalous dispersion curves of negative slope. Therefore, by applying a single-drive field, we can simultaneously control the transparency for two microwave fields when their frequency separation equals $2\omega_g$. Moreover, following Eq. (43), the analytical mean optical response $r_c = -(i\Gamma_d\langle\sigma_-\omega_{pr}\rangle)/(2\Omega_{pr})$ can be approximately expressed as

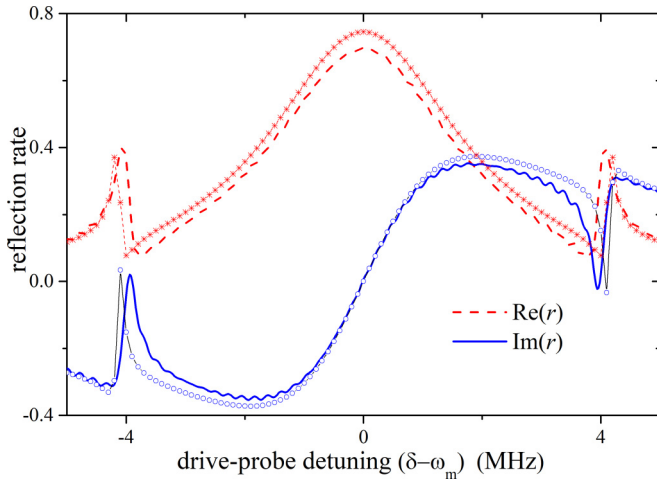$$r_c = \frac{r_{\text{eff}+} + r_{\text{eff}-}}{2}, \quad (44)$$

FIG. 7. Two-color EIT under the condition $\delta_s = 0$. The real and imaginary parts of the reflection coefficient r, Re(r) (red dashed curve) and Im(r) (blue solid curve), versus the drive-probe detuning $(\delta - \omega_m)$ based on our numerical simulations. The analytical average optical response r_c, as given in Eq. (44), is plotted with symbols. Two transparent dips can be found at $\pm\omega_g$. Other parameters adopted here are the same as those in Fig. 4.

which is plotted by the curves with symbols (either stars or circles) in Fig. 7. Interestingly, we find that the analytical results in Eq. (44) can approximately describe the *joint two-color EIT*. The optical response can be viewed as a combined effect of two isolated EIT effects with the same drive detuning, and their interference is negligible, given that $C_{1\pm}$ are much weaker compared with $2\omega_g$. As shown in Eq. (31), the sideband transition C_{1+} is greater than C_{1-}, and the rate difference becomes more apparent when increasing the modulation frequency ω_g. When ω_g is large enough, the two dips in Fig. 7 are not symmetric anymore.

According to Eq. (29), both transition rates C_{1-} and C_{1+} linearly increase with increasing Ω_{drv}. In Fig. 8, we plot the reflection rate Re$[r(\omega_{\mathrm{pr}})]$ as a function of the drive strength Ω_{drv} and probe detuning $(\delta - \omega_m)$. We find that, with increasing Ω_{drv}, the two EIT dips become wider and closer due to strong sideband transition rates $C_{1\pm}$. The two isolated transparent windows affect each other, and they tend to merge. When $C_{1\pm}$ is comparable with the frequency separation $2\omega_g$, the relation $C_{\pm} \ll \omega_g$ is not valid any more, and this two-color EIT almost disappears. If the two sideband transitions are not well separated by frequency detuning, Eq. (44) cannot effectively describe the optical response and the two EIT windows are destroyed.

V. DISCUSSION AND CONCLUSIONS

In this work, we considered a hybrid system consisting of a SQUID embedded with a NAMR. We first showed an example of how to achieve an unconventional parametrically modulated longitudinal interaction between a flux (transmon) qubit and the NAMR. Then, we derived an effective Hamiltonian, which leads to a first-order sideband transition, and found that the coupling modulation significantly changes the dynamics of the hybrid system. A single sideband drive is split under
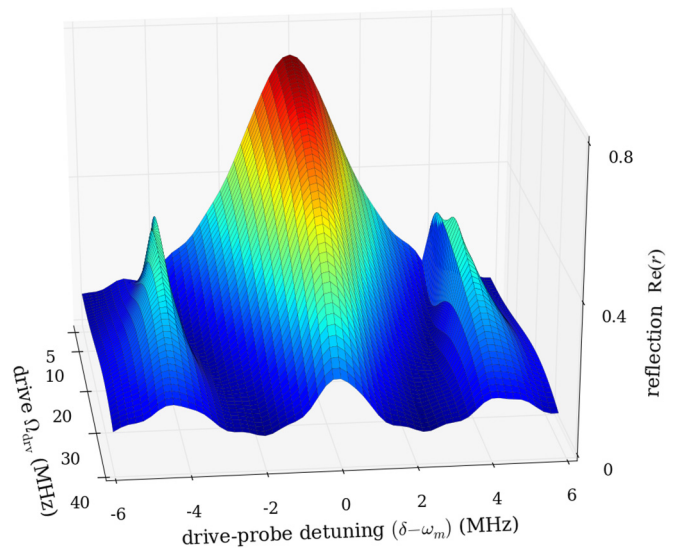

FIG. 8. Real part of the reflection coefficient, Re(r), versus the drive-probe detuning $(\delta - \omega_m)$ and drive strength Ω_{drv} for the two-color EIT. When increasing Ω_{drv}, the two EIT dips located at $\pm\omega_g$ become wider and closer to each other, indicating that the two-color EIT is gradually destroyed by the interference of the two sideband transitions. Other parameters adopted here are the same as those in Fig. 4.

a sinusoidal modulation of the coupling terms. Indeed, the frequency components of the modulation directly determine this splitting. If the modulation is more complex, then more interesting phenomena can be observed.

By applying a resonant probe field, we found that both single- and two-color EIT can be observed. The modulation of the interaction provides another control method for these EIT effects. For the single-color EIT, the drive-probe detuning is not necessarily equal to the NAMR frequency, but can be conveniently tuned by changing the modulation frequency. For the two-color EIT, the double transparent windows occur due to the splitting of sideband transitions and their distance is determined by the modulation frequency. Compared with the usual predictions of two-color EIT in atomic systems, here there is only one drive (control) field. Moreover, it is possible to modify and extend our results to study EIT and Autler-Townes splitting [84,93,94].

As discussed in Ref. [74], for systems with longitudinal interaction, an EIT induced by second-order sideband transitions can also be observed. By considering the modulation of such longitudinal interaction, one might observe multicolor EIT induced by higher-order sideband transitions.

We hope that our results could not only be helpful for studying the dynamics for a system with time-dependent longitudinal coupling, but also can find applications in microwave photonics [9,10] (including vacuum-induced nonlinear optics [40,42]) and quantum information processing [25] with SQCs.

[1] Y. Makhlin, G. Schön, and A. Shnirman, Quantum-state engineering with Josephson-junction devices, Rev. Mod. Phys. **73**, 357 (2001).

[2] M. H. Devoret and J. M. Martinis, Implementing qubits with superconducting integrated circuits, Quantum Inf. Process. **3**, 163 (2004).

[3] J. Q. You and F. Nori, Superconducting circuits and quantum information, Phys. Today **58**(11), 42 (2005).

[4] J. Clarke and F. K. Wilhelm, Superconducting quantum bits, Nature (London) **453**, 1031 (2008).

[5] J. Q. You and F. Nori, Atomic physics and quantum optics using superconducting circuits, Nature (London) **474**, 589 (2011).

[6] I. Buluta, S. Ashhab, and F. Nori, Natural and artificial atoms for quantum computation, Rep. Prog. Phys. **74**, 104401 (2011).

[7] Z. L. Xiang, S. Ashhab, J. Q. You, and F. Nori, Hybrid quantum circuits: Superconducting circuits interacting with other quantum systems, Rev. Mod. Phys. **85**, 623 (2013).

[8] R. J. Schoelkopf and S. M. Girvin, Wiring up quantum systems, Nature (London) **451**, 664 (2008).

[9] X. Gu, A. F. Kockum, A. Miranowicz, Y.-X. Liu, and F. Nori, Microwave photonics with superconducting quantum circuits, Phys. Rep. **718-719**, 1 (2017).

[10] A. F. Kockum, A. Miranowicz, S. De Liberato, S. Savasta, and F. Nori, Ultrastrong coupling between light and matter, arXiv:1807.11636.

[11] J. Johansson, S. Saito, T. Meno, H. Nakano, M. Ueda, K. Semba, and H. Takayanagi, Vacuum Rabi Oscillations in a Macroscopic Superconducting Qubit LC Oscillator System, Phys. Rev. Lett. **96**, 127006 (2006).

[12] L. Garziano, R. Stassi, V. Macrì, A. F. Kockum, S. Savasta, and F. Nori, Multiphoton quantum Rabi oscillations in ultrastrong cavity QED, Phys. Rev. A **92**, 063830 (2015).

[13] K. V. R. M. Murali, Z. Dutton, W. D. Oliver, D. S. Crankshaw, and T. P. Orlando, Probing Decoherence with Electromagnetically Induced Transparency in Superconductive Quantum Circuits, Phys. Rev. Lett. **93**, 087003 (2004).

[14] Z. Dutton, K. V. R. M. Murali, W. D. Oliver, and T. P. Orlando, Electromagnetically induced transparency in superconducting quantum circuits: Effects of decoherence, tunneling, and multilevel crosstalk, Phys. Rev. B **73**, 104516 (2006).

[15] H. Ian, Y.-X. Liu, and F. Nori, Tunable electromagnetically induced transparency and absorption with dressed superconducting qubits, Phys. Rev. A **81**, 063823 (2010).

[16] Y. Chang, T. Shi, Y.-X. Liu, C. P. Sun, and F. Nori, Multistability of electromagnetically induced transparency in atom-assisted optomechanical cavities, Phys. Rev. A **83**, 063826 (2011).

[17] H. Jing, Ş. K. Özdemir, Z. Geng, J. Zhang, X.-Y. Lü, B. Peng, L. Yang, and F. Nori, Optomechanically-induced transparency in parity-time-symmetric microresonators, Sci. Rep. **5**, 9663 (2015).

[18] X. Gu, S.-N. Huai, F. Nori, and Y.-X. Liu, Polariton states in circuit QED for electromagnetically induced transparency, Phys. Rev. A **93**, 063827 (2016).

[19] M. A. Sillanpää, J. Li, K. Cicak, F. Altomare, J. I. Park, R. W. Simmonds, G. S. Paraoanu, and P. J. Hakonen, Autler-Townes Effect in a Superconducting Three-Level System, Phys. Rev. Lett. **103**, 193601 (2009).

[20] J. Li, G. S. Paraoanu, K. Cicak, F. Altomare, J. I. Park, R. W. Simmonds, M. A. Sillanpää, and P. J. Hakonen, Dynamical Autler-Townes control of a phase qubit, Sci. Rep. **2**, 645 (2012).

[21] S. Novikov, J. E. Robinson, Z. K. Keane, B. Suri, F. C. Wellstood, and B. S. Palmer, Autler-Townes splitting in a three-dimensional transmon superconducting qubit, Phys. Rev. B **88**, 060503 (2013).

[22] B. Suri, Z. K. Keane, R. Ruskov, L. S. Bishop, C. Tahan, S. Novikov, J. E. Robinson, F. C. Wellstood, and B. S. Palmer, Observation of Autler–Townes effect in a dispersively dressed Jaynes–Cummings system, New J. Phys. **15**, 125007 (2013).

[23] A. J. Hoffman, S. J. Srinivasan, S. Schmidt, L. Spietz, J. Aumentado, H. E. Türeci, and A. A. Houck, Dispersive Photon Blockade in a Superconducting Circuit, Phys. Rev. Lett. **107**, 053602 (2011).

[24] C. Lang, D. Bozyigit, C. Eichler, L. Steffen, J. M. Fink, A. A. Abdumalikov, M. Baur, S. Filipp, M. P. da Silva, A. Blais, and A. Wallraff, Observation of Resonant Photon Blockade at Microwave Frequencies using Correlation Function Measurements, Phys. Rev. Lett. **106**, 243601 (2011).

[25] G. Wendin, Quantum information processing with superconducting circuits: a review, Rep. Prog. Phys. **80**, 106001 (2017).

[26] J. Q. You and F. Nori, Quantum information processing with superconducting qubits in a microwave field, Phys. Rev. B **68**, 064509 (2003).

[27] M. O. Scully and M. S. Zubairy, *Quantum Optics* (Cambridge University Press, Cambridge, UK, 1997).

[28] Y.-X. Liu, C. P. Sun, and F. Nori, Scalable superconducting qubit circuits using dressed states, Phys. Rev. A **74**, 052321 (2006).

[29] Y.-X. Liu, L. F. Wei, and F. Nori, Generation of nonclassical photon states using a superconducting qubit in a microcavity, EPL **67**, 941 (2004).

[30] J. M. Fink, M. Göppl, M. Baur, R. Bianchetti, P. J. Leek, A. Blais, and A. Wallraff, Climbing the Jaynes–Cummings ladder and observing its nonlinearity in a cavity QED system, Nature (London) **454**, 315 (2008).

[31] M. Hofheinz, E. M. Weig, M. Ansmann, R. C. Bialczak, E. Lucero, M. Neeley, A. D. O'Connell, H. Wang, J. M. Martinis, and A. N. Cleland, Generation of Fock states in a superconducting quantum circuit, Nature (London) **454**, 310 (2008).

[32] H. Wang, M. Hofheinz, M. Ansmann, R. C. Bialczak, E. Lucero, M. Neeley, A. D. O'Connell, D. Sank, J. Wenner, A. N. Cleland, and John M. Martinis, Measurement of the Decay of Fock States

in a Superconducting Quantum Circuit, Phys. Rev. Lett. **101**, 240401 (2008).

[33] A. J. Kerman, Quantum information processing using quasiclassical electromagnetic interactions between qubits and electrical resonators, New J. Phys. **15**, 123011 (2013).

[34] Y.-X. Liu, C.-X. Yang, H.-C. Sun, and X.-B. Wang, Coexistence of single- and multi-photon processes due to longitudinal couplings between superconducting flux qubits and external fields, New J. Phys. **16**, 015031 (2014).

[35] Y. J. Zhao, Y. L. Liu, Y. X. Liu, and F. Nori, Generating nonclassical photon states via longitudinal couplings between superconducting qubits and microwave fields, Phys. Rev. A **91**, 053820 (2015).

[36] S. Richer and D. DiVincenzo, Circuit design implementing longitudinal coupling: A scalable scheme for superconducting qubits, Phys. Rev. B **93**, 134501 (2016).

[37] S. Richer, N. Maleeva, S. T. Skacel, I. M. Pop, and D. DiVincenzo, Inductively shunted transmon qubit with tunable transverse and longitudinal coupling, Phys. Rev. B **96**, 174520 (2017).

[38] R. Stassi and F. Nori, Long-lasting quantum memories: Extending the coherence time of superconducting artificial atoms in the ultrastrong-coupling regime, Phys. Rev. A **97**, 033823 (2018).

[39] A. G. Fowler, M. Mariantoni, J. M. Martinis, and A. N. Cleland, Surface codes: Towards practical large-scale quantum computation, Phys. Rev. A **86**, 032324 (2012).

[40] R. Stassi, V. Macrì, A. F. Kockum, O. Di Stefano, A. Miranowicz, S. Savasta, and F. Nori, Quantum nonlinear optics without photons, Phys. Rev. A **96**, 023818 (2017).

[41] X. Wang, A. Miranowicz, H.-R. Li, and F. Nori, Observing pure effects of counter-rotating terms without ultrastrong coupling: A single photon can simultaneously excite two qubits, Phys. Rev. A **96**, 063820 (2017).

[42] A. F. Kockum, A. Miranowicz, V. Macrì, S. Savasta, and F. Nori, Deterministic quantum nonlinear optics with single atoms and virtual photons, Phys. Rev. A **95**, 063849 (2017).

[43] N. Didier, J. Bourassa, and A. Blais, Fast Quantum Nondemolition Readout by Parametric Modulation of Longitudinal Qubit-Oscillator Interaction, Phys. Rev. Lett. **115**, 203601 (2015).

[44] B. Royer, A. L. Grimsmo, N. Didier, and A. Blais, Fast and high-fidelity entangling gate through parametrically modulated longitudinal coupling, Quantum **1**, 11 (2017).

[45] J.-Q. Liao and L. Tian, Macroscopic Quantum Superposition in Cavity Optomechanics, Phys. Rev. Lett. **116**, 163602 (2016).

[46] M. Cirio, K. Debnath, N. Lambert, and F. Nori, Amplified Optomechanical Transduction of Virtual Radiation Pressure, Phys. Rev. Lett. **119**, 053601 (2017).

[47] O. Shevchuk, G. A. Steele, and Y. M. Blanter, Strong and tunable couplings in flux-mediated optomechanics, Phys. Rev. B **96**, 014508 (2017).

[48] J. Wang, Y.-F. Zhu, K. J. Jiang, and M. S. Zhan, Bichromatic electromagnetically induced transparency in cold rubidium atoms, Phys. Rev. A **68**, 063810 (2003).

[49] H. Wang, X. Gu, Y.-X. Liu, A. Miranowicz, and F. Nori, Optomechanical analog of two-color electromagnetically induced transparency: Photon transmission through an optomechanical device with a two-level system, Phys. Rev. A **90**, 023817 (2014).

[50] H. Yan, K.-Y. Liao, J.-F. Li, Y.-X. Du, Z.-M. Zhang, and S.-L. Zhu, Bichromatic electromagnetically induced transparency in hot atomic vapors, Phys. Rev. A **87**, 055401 (2013).

[51] Z.-B. Wang, K.-P. Marzlin, and B. C. Sanders, Large Cross-Phase Modulation between Slow Copropagating Weak Pulses in ^{87}Rb, Phys. Rev. Lett. **97**, 063901 (2006).

[52] S. A. Moiseev and B. S. Ham, Quantum manipulation of two-color stationary light: Quantum wavelength conversion, Phys. Rev. A **73**, 033812 (2006).

[53] M. Bajcsy, S. Hofferberth, V. Balic, T. Peyronel, M. Hafezi, A. S. Zibrov, V. Vuletic, and M. D. Lukin, Efficient All-Optical Switching using Slow Light within a Hollow Fiber, Phys. Rev. Lett. **102**, 203902 (2009).

[54] K.-Y. Xia and J. Twamley, All-Optical Switching and Router via the Direct Quantum Control of Coupling between Cavity Modes, Phys. Rev. X **3**, 031013 (2013).

[55] I.-C. Hoi, C. M. Wilson, G. Johansson, T. Palomaki, B. Peropadre, and P. Delsing, Demonstration of a Single-Photon Router in the Microwave Regime, Phys. Rev. Lett. **107**, 073601 (2011).

[56] P. M. Leung and B. C. Sanders, Coherent Control of Microwave Pulse Storage in Superconducting Circuits, Phys. Rev. Lett. **109**, 253603 (2012).

[57] L. He, Y.-X. Liu, S. Yi, C. P. Sun, and F. Nori, Control of photon propagation via electromagnetically induced transparency in lossless media, Phys. Rev. A **75**, 063818 (2007).

[58] Y.-X. Liu, X.-W. Xu, A. Miranowicz, and F. Nori, From blockade to transparency: Controllable photon transmission through a circuit-qed system, Phys. Rev. A **89**, 043818 (2014).

[59] M. D. Lukin and A. Imamoglu, Nonlinear Optics and Quantum Entanglement of Ultraslow Single Photons, Phys. Rev. Lett. **84**, 1419 (2000).

[60] S.-J. Li, X.-D. Yang, X.-M. Cao, C.-H. Zhang, C.-D. Xie, and H. Wang, Enhanced Cross-Phase Modulation Based on a Double Electromagnetically Induced Transparency in a Four-Level Tripod Atomic System, Phys. Rev. Lett. **101**, 073602 (2008).

[61] S. Etaki, M. Poot, I. Mahboob, K. Onomitsu, H. Yamaguchi, and H. S. J. van der Zant, Motion detection of a micromechanical resonator embedded in a d.c. SQUID, Nat. Phys. **4**, 785 (2008).

[62] M. Poot, S. Etaki, I. Mahboob, K. Onomitsu, H. Yamaguchi, Ya. M. Blanter, and H. S. J. van der Zant, Tunable Backaction of a DC SQUID on an Integrated Micromechanical Resonator, Phys. Rev. Lett. **105**, 207203 (2010).

[63] S. Etaki, F. Konschelle, Ya. M. Blanter, H. Yamaguchi, and H. S. J. van der Zant, Self-sustained oscillations of a torsional SQUID resonator induced by Lorentz-force back-action, Nat. Commun. **4**, 1803 (2013).

[64] B. H. Schneider, S. Etaki, H. S. J. van der Zant, and G. A. Steele, Coupling carbon nanotube mechanics to a superconducting circuit, Sci. Rep. **2**, 599 (2012).

[65] M. J. Schwarz, Gradiometric tunable-gap flux qubits in a circuit QED architecture, Ph.D. thesis, Technische Universität München, München, 2015.

[66] F. Xue, Y.-X. Liu, C. P. Sun, and F. Nori, Two-mode squeezed states and entangled states of two mechanical resonators, Phys. Rev. B **76**, 064305 (2007).

[67] F. Xue, Y. D. Wang, C. P. Sun, H. Okamoto, H. Yamaguchi, and K. Semba, Controllable coupling between flux qubit and nanomechanical resonator by magnetic field, New J. Phys. **9**, 35 (2007).

[68] F. G. Paauw, A. Fedorov, C. J. P. M Harmans, and J. E. Mooij, Tuning the Gap of a Superconducting Flux Qubit, Phys. Rev. Lett. **102**, 090501 (2009).

[69] F. G. Paauw, Superconducting flux qubits: Quantum chains and tunable qubits, Ph.D. thesis, Technische Universiteit Delft, Delft, 2009.

[70] A. Fedorov, A. K. Feofanov, P. Macha, P. Forn-Díaz, C. J. P. M. Harmans, and J. E. Mooij, Strong Coupling of a Quantum Oscillator to a Flux Qubit at its Symmetry Point, Phys. Rev. Lett. **105**, 060503 (2010).

[71] M. Stern, G. Catelani, Y. Kubo, C. Grezes, A. Bienfait, D. Vion, D. Esteve, and P. Bertet, Flux Qubits with Long Coherence Times for Hybrid Quantum Circuits, Phys. Rev. Lett. **113**, 123601 (2014).

[72] J. E. Mooij, T. P. Orlando, L. Levitov, L. Tian, C. H. van der Wal, and S. Lloyd, Josephson persistent-current qubit, Science **285**, 1036 (1999).

[73] T. P. Orlando, J. E. Mooij, L. Tian, C. H. van der Wal, L. S. Levitov, S. Lloyd, and J. J. Mazo, Superconducting persistent-current qubit, Phys. Rev. B **60**, 15398 (1999).

[74] X. Wang, A. Miranowicz, H.-R. Li, and F. Nori, Hybrid quantum device with a carbon nanotube and a flux qubit for dissipative quantum engineering, Phys. Rev. B **95**, 205415 (2017).

[75] J. Koch, T. M. Yu, J. Gambetta, A. A. Houck, D. I. Schuster, J. Majer, A. Blais, M. H. Devoret, S. M. Girvin, and R. J. Schoelkopf, Charge-insensitive qubit design derived from the Cooper pair box, Phys. Rev. A **76**, 042319 (2007).

[76] J. Q You, X. Hu, S. Ashhab, and F. Nori, Low-decoherence flux qubit, Phys. Rev. B **75**, 140515 (2007).

[77] J. A. Schreier, A. A. Houck, J. Koch, D. I. Schuster, B. R. Johnson, J. M. Chow, J. M. Gambetta, J. Majer, L. Frunzio, M. H. Devoret, S. M. Girvin, and R. J. Schoelkopf, Suppressing charge noise decoherence in superconducting charge qubits, Phys. Rev. B **77**, 180502 (2008).

[78] F. Mallet, F. R. Ong, A. Palacios-Laloy, F. Nguyen, P. Bertet, D. Vion, and D. Esteve, Single-shot qubit readout in circuit quantum electrodynamics, Nat. Phys. **5**, 791 (2009).

[79] Z. Yao, C. L. Kane, and C. Dekker, High-Field Electrical Transport in Single-Wall Carbon Nanotubes, Phys. Rev. Lett. **84**, 2941 (2000).

[80] A. K. Hüttel, G. A. Steele, B. Witkamp, M. Poot, L. P. Kouwenhoven, and H. S. J. van der Zant, Carbon nanotubes as ultrahigh quality factor mechanical resonators, Nano Lett. **9**, 2547 (2009).

[81] E. A. Laird, F. Pei, W. Tang, G. A. Steele, and L. P. Kouwenhoven, A high quality factor carbon nanotube mechanical resonator at 39 GHz, Nano Lett. **12**, 193 (2011).

[82] A. Benyamini, A. Hamo, S. V. Kusminskiy, F. von Oppen, and S. Ilani, Real-space tailoring of the electron-phonon coupling in ultraclean nanotube mechanical resonators, Nat. Phys. **10**, 151 (2014).

[83] O. Astafiev, A. M. Zagoskin, A. A. Abdumalikov, Yu. A. Pashkin, T. Yamamoto, K. Inomata, Y. Nakamura, and J. S. Tsai, Resonance fluorescence of a single artificial atom, Science **327**, 840 (2010).

[84] P. M. Anisimov, J. P. Dowling, and B. C. Sanders, Objectively Discerning Autler-Townes Splitting from Electromagnetically Induced Transparency, Phys. Rev. Lett. **107**, 163604 (2011).

[85] I.-C. Hoi, T. Palomaki, J. Lindkvist, G. Johansson, P. Delsing, and C. M. Wilson, Generation of Nonclassical Microwave States using an Artificial Atom in 1D Open Space, Phys. Rev. Lett. **108**, 263601 (2012).

[86] X. Wang, H. R. Li, D. X. Chen, W. X. Liu, and F. L. Li, Tunable electromagnetically induced transparency in a composite superconducting system, Opt. Commun. **366**, 321 (2016).

[87] A. A. Abdumalikov, O. Astafiev, A. M. Zagoskin, Yu. A. Pashkin, Y. Nakamura, and J. S. Tsai, Electromagnetically Induced Transparency on a Single Artificial Atom, Phys. Rev. Lett. **104**, 193601 (2010).

[88] M. Fleischhauer, A. Imamoglu, and J. P. Marangos, Electromagnetically induced transparency: Optics in coherent media, Rev. Mod. Phys. **77**, 633 (2005).

[89] C. P. Sun, L. F. Wei, Y.-X. Liu, and F. Nori, Quantum transducers: Integrating transmission lines and nanomechanical resonators via charge qubits, Phys. Rev. A **73**, 022318 (2006).

[90] J. Moser, A. Eichler, J. Güttinger, M. I. Dykman, and A. Bachtold, Nanotube mechanical resonators with quality factors of up to 5 million, Nat. Nanotechnol. **9**, 1007 (2014).

[91] J.-J. Li and K.-D. Zhu, Tunable slow and fast light device based on a carbon nanotube resonator, Opt. Express **20**, 5840 (2012).

[92] Y. Liu, J.-H. Wu, D.-S. Ding, B.-S. Shi, and G.-C. Guo, Bichromatic field generation from double-four-wave mixing in a double-electromagnetically induced transparency system, New J. Phys. **14**, 073047 (2012).

[93] B. Peng, Ş. K. Özdemir, W.-J. Chen, F. Nori, and L. Yang, What is and what is not electromagnetically induced transparency in whispering-gallery microcavities, Nat. Commun. **5**, 5082 (2014).

[94] H.-C. Sun, Y.-X. Liu, H. Ian, J. Q. You, E. Il'ichev, and F. Nori, Electromagnetically induced transparency and Autler-Townes splitting in superconducting flux quantum circuits, Phys. Rev. A **89**, 063822 (2014).